



## Direct Observation of Fractal-Dimensional Percolation in the 3D Cluster Dynamics of a Ferroelectric Supercrystal

Ludovica Falsi,<sup>1,2,\*</sup> Marco Aversa<sup>1</sup>,, Fabrizio Di Mei,<sup>1</sup> Davide Pierangeli,<sup>1</sup> Feifei Xin,<sup>1,3</sup> Aharon J. Agranat<sup>4</sup>,, and Eugenio DelRe<sup>1,5</sup>

<sup>1</sup>*Dipartimento di Fisica, Università di Roma “La Sapienza,” 00185 Rome, Italy*

<sup>2</sup>*Dipartimento S.B.A.I., Sezione di Fisica, “Sapienza” Università di Roma, I-00161 Roma, Italy*

<sup>3</sup>*College of Physics and Materials Science, Tianjin Normal University, 300387 Tianjin, China*

<sup>4</sup>*The Brojde Center for Innovative Engineering and Computer Science, The Hebrew University, Jerusalem 91904, Israel*

<sup>5</sup>*ISC-CNR, Università di Roma “La Sapienza,” 00185 Rome, Italy*



(Received 24 August 2020; accepted 7 December 2020; published 21 January 2021)

We perform percolation analysis of crossed-polarizer transmission images in a biased nanodisordered bulk KTN:Li perovskite. Two distinct percolative transitions are identified at two electric field thresholds. The low-field transition involves a directional fractal chain of dimension  $\mathcal{D} = 1.65$ , while the high-field transition has a dimension  $\mathcal{D} > 2$ . Direct cluster imaging in the volume is achieved using high-resolution orthographic 3D projections based on giant refraction. Percolation is attributed to a full-3D domain reorientation that mediates the transition from a ferroelectric supercrystal state to a disordered domain mosaic.

DOI: [10.1103/PhysRevLett.126.037601](https://doi.org/10.1103/PhysRevLett.126.037601)

A basic open question is if a general class of dynamics exists at the microscopic scale that characterizes the transition of a system from one macroscopic state to another. While continuous phase transitions are macroscopically characterized by universal power laws that can be deduced from scale invariance in their statistical field description, no analogous universality is known to exist in the microscopic details of how the transition occurs, i.e., in its underlying space-time dynamics [1]. The issue has been investigated in ferroelectrics, where the transition is from a nonpolar or paraelectric crystal state to a polar ferroelectric one [2,3]. One candidate microscopic process driving the transition is polar cluster percolation [4,5], a mechanism that, being self-similar, has intriguing and hereto unexplored similarities to statistical scale invariance [6]. Ferroelectrics form an ideal setting for the study of percolation. For one, the process is triggered by changes in the average cluster size and can therefore be activated by changes in temperature, pressure, and external electric fields. Furthermore, since ferroelectrics naturally form bulk macroscopic crystals, percolation can be analyzed in a full-3D environment, that is, for clusters that interact and reorient in all three spatial directions [7–11].

Dielectric spectroscopy has allowed the indirect identification of percolation in ferroelectric transitions of bulk crystals [12]. Direct evidence of percolation dynamics in a full-3D geometry is not yet available. The basic experimental difficulty lies in extracting geometrical cluster data from a volume for different external parameters. While the microscopic details of a percolation can be observed from a volume by sectioning the sample and scanning the surface

[13,14], a full statistical analysis as a function of temperature and electric bias requires a noninvasive imaging approach. Ferroelectric clusters can be optically imaged using crossed polarizers [15], a technique based on the fact that a polar cluster can change the state of polarization of propagating light due to its birefringence. The problem is that each single cluster can form in a volume with a size that can range from tens to hundreds of nanometers. This makes direct wide-area imaging generally unfeasible, as the clusters can occupy any position in the volume and transmitted light will normally pass through different arbitrarily oriented domains. Recent studies have shown that some ferroelectrics form highly organized 3D cluster distributions called ferroelectric supercrystals (SCs) [16–20]. Light propagating through these suffers a broadband giant refraction (GR) [21]: waves travel along the principal axes of the crystal without diffracting and separating into polarization maintaining components [22], amounting to a natural 3D orthographic projection. This opens up the possibility of observing optically the microscopic details of SC cluster percolation even though it is taking place on the micrometer scale in a full-3D volume.

In this Letter, we use GR to perform, for the first time, direct imaging of ferroelectric cluster dynamics. Experiments are performed in ferroelectric KTN:Li, kept at a few degrees below its Curie point and subjected to an external electric field. The analysis of polarization transmission images through the sample versus electric field indicate a low-dimensional fractal percolation followed by a second high-dimensional percolation as the sample undergoes a transition from the highly organized SC state

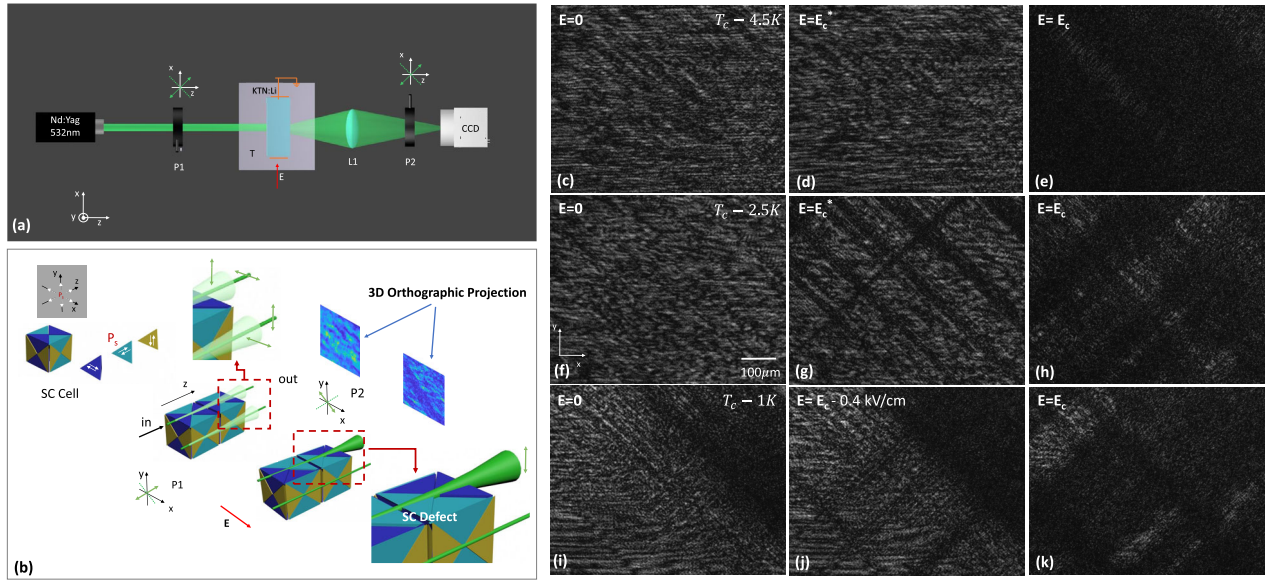


FIG. 1. Direct imaging of SC ferroelectric cluster dynamics. (a) Experimental setup. (b) 3D orthographic crossed-polarizer projection technique (see text). (c)–(k) Crossed-polarizer transmission microscopy images in various conditions of temperature and bias electric field (see text).

at zero applied field to a disordered ferroelectric cluster state. The phenomenon is associated with the specific anisotropic features of the field-induced breakdown of the full-3D vortexlike polarization structures underlying the SC.

The experimental setup is illustrated in Fig. 1(a). Laser light ( $\lambda = 532$  nm) is made to propagate along the  $z$  axis through the zero-cut KTN:Li crystal sandwiched between two crossed polarizers (P1 and P2). The  $2.33(x) \times 1.96(y) \times 2.03(z)$  mm<sup>3</sup> sample has an average composition  $\text{K}_{0.997}\text{Ta}_{0.64}\text{Nb}_{0.36}\text{O}_3:\text{Li}_{0.003}$  and is biased by a time-constant electric field  $E$  along the  $x$  axis. Crystal temperature  $T$  is set by a current-controlled Peltier junction in contact with one of the  $y$  facets. Light from the crystal output facet is imaged by a lens (L1) that forms an image of the output crystal plane onto the front-view charge coupled device camera.

The 3D orthographic cross-polarizer projection technique that allows the observation of cluster percolation is illustrated in Fig. 1(b). The fundamental cell of the SC is illustrated in Fig. 1(b) (top left panels): a total of 24 ferroelectric domains are interlocked together forming a cubic structure, where four domains have a spontaneous polarization ( $\mathbf{P}_s$ , white arrows) oriented along one of the six specific directions compatible with the tetragonal phase. The domains can then be classified into three different classes: those with spontaneous polarization parallel to the  $x$  axis (blue), to the  $y$  axis (yellow), and to the  $z$  axis (light blue). As illustrated in the central panel, light propagating with a linear polarization (green double-arrow) at  $45^\circ$  with respect to the  $x$  and  $y$  axes (as transmitted by polarizer P1) will suffer GR only for the component of the polarization

parallel to the local spontaneous polarization  $\mathbf{P}_s$ . For each SC cell, this field component will propagate with negligible diffraction along the  $z$  axis of the sample normal to the input facet (dark-green component), while the component of the field with a polarization orthogonal to the local SC spontaneous polarization will suffer standard diffraction and refraction [22] (light-green component). The transmitted light at output will then be a checkerboardlike polarization pattern, with an alternating linear polarization parallel to the  $x$  and  $y$  axes, superimposed on a diffracted background component with a polarization parallel to the input polarization. The output linear polarizer P2, oriented so as to allow light polarized orthogonal to the input linear polarization to pass, will then block the component not suffering GR and allow the transmission of 50% of the component suffering GR. The situation is altered when the sample is subject to an external electric field  $E$  directed along a crystal principal axis [bias field red arrow in Fig. 1(b)]. The vortex structure, now subject to a directional ( $x$ -directed) stimulus, undergoes a characteristic distortion [SC defect in Fig. 1(b)] [23]. The result is that the specific portion of the field undergoing GR that encounters the defect in the volume finds itself with a polarization that no longer supports GR, diffracts, and leads to a dark region in the transmission pattern. The region is, in turn, still well defined in the transmission image, as the cells supporting GR that surround it allow light to proceed undistorted and unaffected to the output [right panel in Fig. 1(b)].

Basic phenomenology is reported in Fig. 1(c)–(k), where polarization transmission images through the sample are shown for various temperatures below  $T_C = 294$  K. As reported in Fig. 1(c)–(e), for temperatures deep into the

ferroelectric phase ( $T = T_C - 4.5$  K), crossed-polarizer images indicate the existence of a single bias-induced transition at  $E_c = 2.85$  kV/cm, with no specific anisotropic features. At this critical field, the crossed-polarizer image becomes wholly opaque, and hence the SC structure, which generates an overall unpolarized transmitted beam, is lost. A very different picture emerges at  $T = T_C - 2.5$  K, as reported in Fig. 1(f)–(h). Here at the field value  $E_c^* = 2.45$  kV/cm crossed-polarizer transmission begins to decrease along specific directions at  $45^\circ$  with respect to the crystal  $x$  and  $y$  axes. The SC structure appears to suffer bias-induced distortions preferentially along these slanted directions. The overall picture still allows light transmission [Fig. 1(g)]. Increasing the bias field further, the dark regions grow along the oriented directions and ultimately expand to encompass the entire transmitted image at  $E_c = 2.80$  kV/cm [Fig. 1(h)]. In turn, even closer to the Curie point, at  $T = T_C - 1.0$  K [Fig. 1(i)–(k)], the two-step dynamic is no longer discernible [Fig. 1(j)], and a single fully dark transmission intervenes above  $E_c = 2.40$  kV/cm [Fig. 1(k)].

Percolation analysis of the transition from a regime of light transmission to one of no light transmission through the cross polarizers, associated with the breakdown of the SC structure, is reported in Fig. 2. Observed images [Fig. 2(a)–(c)] are processed for analysis. In order to delineate the percolative region, we first binarize the collected images, selecting a threshold intensity: a pixel is considered to be in state 1 if it has an intensity lower than

the threshold and in state 0 otherwise. The threshold intensity is taken to be the background intensity of the unbiased SC pattern [average intensity of the dark regions in Fig. 2(a)]. To identify the clusters' size in the binarized transmission images, we define connected pixels that make up a cluster using the Von Neumann neighborhood criterium: square-shaped pixels are considered connected when they share their binarized state along an edge, while pixels that share a vertex, i.e., are adjacent and have the same state along the diagonal of the pixel lattice, are not considered connected. The processed images thus partitioned into clusters are reported in Fig. 2(d)–(f). Now the mean cluster size  $S$  (system susceptibility) is defined as  $S = \sum_s w_s s$ , where  $w_s$  is the probability that an image pixel belongs to a cluster of size  $s$  (the ratio of the number of pixels belonging to clusters of size  $s$  divided by the total number of pixels). A cluster is taken to be percolating (the infinite cluster) when it is found to spread from one external boundary of the processed image to another, as occurring in the  $x$ - $y$  direction for the anisotropic dynamics of Fig. 2(e) and Fig. 2(f). For this cluster, we then determined its so-called strength  $P_\infty = n_\infty/N$ , where  $n_\infty$  is the number of pixels in state 1 that belong to it and  $N$  the total number of pixels in the processed image. Dynamics are analyzed in terms of the composition  $p$ , i.e., the probability that a site in the lattice is in state 1. In these terms, the average cluster size will diverge following the power law  $|p_c - p|^{-\gamma}$  at the percolation threshold  $p_c$ , and  $P_\infty$  will grow for a composition above  $p_c$  as  $(p - p_c)^\beta$  [6]. The exponents  $\gamma$  and  $\beta$  depend on the dimensionality and type of underlying lattice [6].

Results for  $S$  are reported in Fig. 2(g) as a function of bias electric field  $E$ . Fitting the data with a  $|E_c - E|^{-\gamma}$  law gives a critical exponent  $\gamma = 1.24 \pm 0.10$  and  $E_c = 2.82$  kV/cm. Cluster strength  $P_\infty$  versus  $E$  is reported in Fig. 2(h). Data can be fitted for fields  $E > E_c^*$  by  $(E - E_c^*)^\beta$ , with  $\beta = 0.67 \pm 0.05$  and  $E_c^* = 2.45$  kV/cm, i.e., with a threshold field  $E_c^* \neq E_c$ . This signals the existence of two distinct percolative transitions, the lower field transition occurring at  $E_c^*$ , preferentially along directions at  $45^\circ$  relative to the principal  $x$  and  $y$  axis [Fig. 2(e)], and the isotropic transition occurring at the higher field  $E_c$ . In Fig. 2(i) we report the mean cluster  $S$  at the critical value  $E_c$  as a function of the length scale  $L$ . Results are fitted by a power law for  $L > 20 \mu\text{m}$  (1 pixel =  $0.5 \mu\text{m}$ ), with an exponent  $\gamma/\nu = 1.94 \pm 0.10$ . The result is in agreement with predictions for finite-system susceptibility at the percolation critical point that scales as  $S \propto L^{\gamma/\nu}$ , where  $L$  is the size of the system [24]. Percolation analysis is consistent with results obtained in [4] for electric field-induced percolation in  $\text{Ba}(\text{Zr}, \text{Ti})\text{O}_3$  and also with values assumed in [5] for temperature-induced percolation in  $\text{Pb}(\text{Mg}, \text{Nb})\text{O}_3$ .

A basic consequence of the appearance of critical exponent behavior is that the field-induced transition from

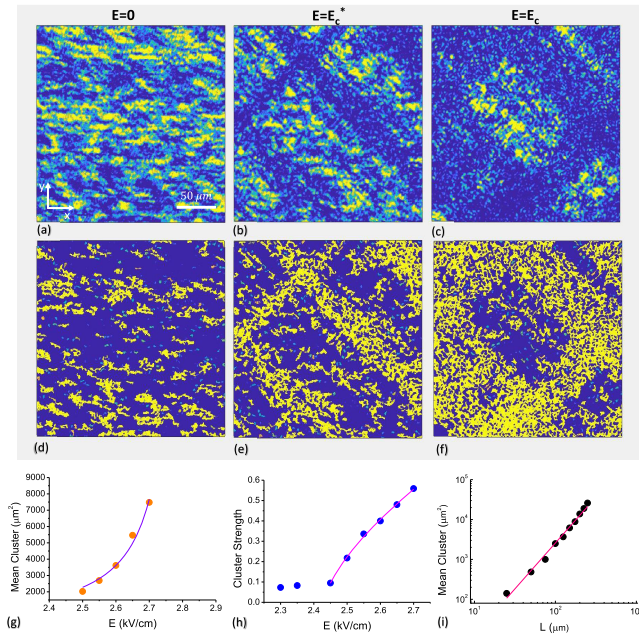


FIG. 2. Percolation analysis of SC breakdown. (a)–(c) Crossed-polarizer wide-area transmission images for different bias electric fields at  $T_C - 2.5$  K and (d)–(f) binarization (see text). (g)–(i) Critical exponent analysis (see text).

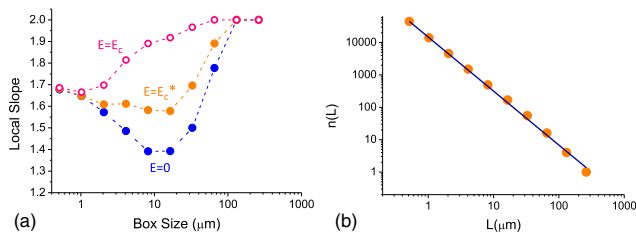


FIG. 3. Fractal dimensional nature of the percolation. (a) Local slope versus box size. (b) Number of boxes needed to cover the set as a function of the size of the boxes of  $L$  (see text).

the SC state is characterized by scale invariance, a feature it shares with conventional phase transitions. In turn, percolation also manifest self-similarity by which the actual geometry of the percolating cluster is the same as seen on different magnification scales. In these terms, the size of the largest cluster will in general scale  $\propto L^D$ , with  $D < d$ , i.e., smaller than the spatial dimension of the hosting space ( $d = 3$ ). Since we are observing the 2D projection of the cluster percolation, we can measure the fractal dimension of the percolating cluster only for  $D < 2$  [25–27]. In Fig. 3, we provide a Kolmogorov capacity analysis of the transmission images using the box counting method [25,28]. As reported in Fig. 3(a), while for fields above and below the threshold field  $E_c^*$  the local slope changes for different box scales, for  $E \simeq E_c^*$  it has an almost constant value, as expected for a fractal-dimensional percolation. As reported in Fig. 3(b), fitting the number of boxes  $n(L) \propto L^{-D}$  needed to cover the infinite cluster  $P_\infty$  versus the length scale  $L$  gives a fractal dimension  $D = 1.65$  ( $D < 2$ ). Interestingly, the observed fractal dimension is in agreement with interpretative models of dielectric spectroscopy response in analogous materials and, indeed, with numerical simulations of other complex relaxor materials [12,29]. In turn, fractal-dimensional analysis of the second percolative process associated with  $E_c$  yields  $D = 2$ , so that the fractal nature of this second transition cannot be detected in our (projective) setup.

The interpretation of results can be formulated assuming the 3D vortex structure of a ferroelectric SC, as originally formulated in Ref. [21]. In the 3D SC matrix, illustrated in Fig. 4(a), the application of an external bias electric field

will then distort the domain mosaic in a dominolike effect: the defect will propagate along the diagonal direction, as schematically illustrated in Fig. 4(b). Since the defect in general enucleates inside the unperturbed SC in a random position in the volume along the  $z$  axis, this will cause a dark region in the crossed-polarizer images [Fig. 4(c),(d)]. Hence, once the first percolation transition is reached at  $E_c^*$ , the diagonal defects that cause dark regions in the transmitted image expand from one edge of the investigated volume to the other. In turn, the second percolative transition occurs as all the tassels in the mosaic align with the external field, a condition in which the entire transmitted image becomes darker. The percolative chain, as in Fig. 4(b), forming at a given position  $z^*$  along the propagation axis  $z$ , will halt GR at that  $z^*$  and cause the light originally transmitted by that specific SC cell to diffract and be blocked by the output polarizer [Fig. 4(d)]. The effects of SC percolative breakdown on GR for focused light beams is analyzed using a high-aperture long-working distance microscope objective (OBJ, Edmund Optics - 100X- 3 mm working distance -achromatic-NA = 0.8). While the sample is optically transparent above  $T_C$  (absorption coefficient  $\alpha \simeq 2 \text{ cm}^{-1}$ ), scattering associated with ferroelectric clustering increases below  $T_C$  ( $\alpha \simeq 10 \text{ cm}^{-1}$  at  $T_C - 4.5 \text{ K}$ ). This allows the observation of beam dynamics inside the sample through top-view images of stray scattering, as reported in Fig. 5. An important parameter to separate light undergoing GR from light not suffering GR in top-view experiments is the rotation angle of the KTN:Li sample around the vertical  $y$  axis,  $\theta$  (see Fig. 5, first panel), i.e., the angle between the normal to the sample input facet ( $z$ ) and the experiment propagation axis ( $z'$ ). The breakdown of GR for  $E > 2.50 \text{ kV/cm}$  coincides with the onset of cluster percolations.

These findings shed light on the nature and susceptibility of ferroelectric supercrystals [16–22,30,31]. They suggest a specific role for organized 3D polarization structures below the Curie temperature [32–34]. Three-dimensional polarization vortices can have profound repercussions on our understanding of volume samples and the development of future energy and information storing technology [35,36].

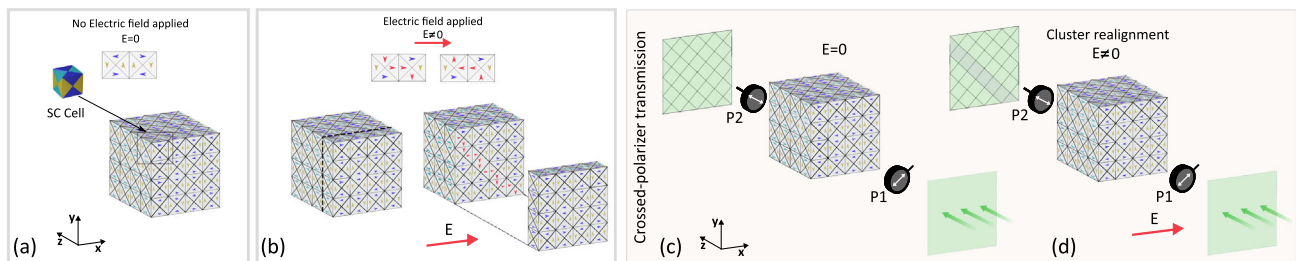


FIG. 4. Percolation picture in a biased SC. (a),(b) Illustration of directional percolation and (c),(d) its effect on crossed-polarizer transmission (see text).

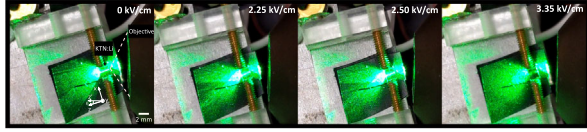


FIG. 5. Top-view images of scattered light across the percolative transition (see text).

In conclusion, we analyze the effects of a constant external bias electric field on a ferroelectric supercrystal. While the crystal is transparent, crossed-polarizer transmission images have a characteristic disordered nature whose statistical analysis signals the existence of percolative cluster dynamics. Giant refraction causes light naturally to form orthographic projections and allows us to identify two distinct percolative processes that occur in the 3D volume. The first is a fractional-dimensional percolation with a dimension of  $\mathcal{D} = 1.65$ , while the second has a dimension of  $\mathcal{D} > 2$ . Phenomenology is interpreted in terms of biased vortex geometries in a full 3D mosaic and forms further evidence of the role played by 3D vortices in the mesoscopic physics of solid-solution ferroelectrics cooled below their Curie point. In more general terms, the direct observation, in the transparent volume, of percolating cluster dynamics sheds light on the microscopic origins of self-similarity in natural 3D systems.

We acknowledge support from the PRIN 2017 PELM project (Grant No. 20177PSCKT), the “Attract” project funded by the EC under Grant Agreement No. 777222, the Sapienza-Ricerca di Ateneo 2019 project, the H2020 Fet project PhoQus, and the Israel Science Foundation (Grant No. 1960/16). Ministero dell’Istruzione, dell’Università e della Ricerca

\*Corresponding author.

ludovica.falsi@uniroma1.it

- [1] J. P. Bouchaud, Weak ergodicity breaking and aging in disordered systems, *J. Phys. I (France)* **2**, 1705 (1992).
- [2] V. Wadhawan, *Introduction to Ferroic Materials* (CRC Press, London, 2000).
- [3] K. M. Rabe, C. H. Ahn, and J. M. Triscone, *Physics of Ferroelectrics: A Modern Perspective* (Springer, New York, 2007), Vol. 105.
- [4] S. Prosandeev, D. Wang, A. R. Akbarzadeh, B. Dkhil, and L. Bellaiche, Field-Induced Percolation of Polar Nanoregions in Relaxor Ferroelectrics, *Phys. Rev. Lett.* **110**, 207601 (2013).
- [5] R. Pirc and R. Blinc, Vogel-Fulcher freezing in relaxor ferroelectrics, *Phys. Rev. B* **76**, 020101(R) (2007).
- [6] D. Stauffer and A. Aharony, *Introduction To Percolation Theory*, 2nd ed. (Taylor & Francis, New York, 1992).
- [7] A. L. Roytburd, S. P. Alpay, L. A. Bendersky, V. Nagarajan, and R. Ramesh, Three-domain architecture of stress-free epitaxial ferroelectric films, *J. Appl. Phys.* **89**, 553 (2001).
- [8] N. T. Tsou, P. R. Potnis, and J. E. Huber, Classification of laminate domain patterns in ferroelectrics, *Phys. Rev. B* **83**, 184120 (2011).
- [9] Y. Nahas, S. Prokhorenko, L. Louis, Z. Gui, I. Kornev, and L. Bellaiche, Discovery of stable skyrmionic state in ferroelectric nanocomposites, *Nat. Commun.* **6**, 8542 (2015).
- [10] S. Prosandeev, B. Xu, and L. Bellaiche, Polarization switching in the  $\text{PbMg}_{1/3}\text{Nb}_{2/3}\text{O}_3$  relaxor ferroelectric: An atomistic effective Hamiltonian study, *Phys. Rev. B* **98**, 024105 (2018).
- [11] I. Muench, A. R. Balakrishna, and J. E. Huber, Periodic boundary conditions for the simulation of 3D domain patterns in tetragonal ferroelectric material, *Arch. Appl. Mech.* **89**, 955972 (2019).
- [12] S. E. Lerner, P. B. Ishai, A. J. Agranat, and Y. Feldman, Percolation of polar nanoregions: A dynamic approach to the ferroelectric phase transition, *J. Non-Cryst. Solids* **353**, 4422 (2007).
- [13] R. Viswanathan and M. B. Heaney, Direct Imaging of the Percolation Network in a Three-Dimensional Disordered Conductor-Insulator Composite, *Phys. Rev. Lett.* **75**, 4433 (1995).
- [14] N. Shimoni, D. Azulai, I. Balberg, and O. Millo, Tomographic-like reconstruction of the percolation cluster as a phase transition, *Phys. Rev. B* **66**, 020102(R) (2002).
- [15] H. Tian, B. Yao, L. Wang, P. Tan, X. Meng, G. Shi, and Z. Zhou, Dynamic response of polar nanoregions under an electric field in a paraelectric  $\text{KTA}_{0.61}\text{Nb}_{0.39}\text{O}_3$  single crystal near the para-ferroelectric phase boundary, *Sci. Rep.* **5**, 13751 (2015).
- [16] D. Pierangeli, M. Ferraro, F. Di Mei, G. Di Domenico, C. E. M. de Oliveira, A. J. Agranat, and E. DelRe, Supercrystals in composite ferroelectrics, *Nat. Commun.* **7**, 10674 (2016).
- [17] L. Falsi, L. Tartara, F. Di Mei, M. Flammini, J. Parravicini, D. Pierangeli, G. Parravicini, F. Xin, P. DiPorto, A. J. Agranat, and E. DelRe, Constraint-free wavelength conversion supported by giant optical refraction in a 3D perovskite supercrystal, *Commun. Mater.* **1**, 76 (2020).
- [18] C. Li, X. Wang, Y. Wu, F. Liang, F. Wang, X. Zhao, H. Yu, and H. Zhang, Three-dimensional nonlinear photonic crystal in naturally grown potassium-tantalate-niobate perovskite ferroelectrics, *Light Sci. Appl.* **9**, 193 (2020).
- [19] L. Lo Presti, J. Parravicini, R. Soave, G. Parravicini, M. Mauri, L. Loconte, F. Di Mei, L. Falsi, L. Tartara, S. Binetti, A. J. Agranat, and E. DelRe, Observation of an exotic lattice structure in the transparent  $\text{KTA}_{1-x}\text{Nb}_x\text{O}_3$  perovskite supercrystal, *Phys. Rev. B* **102**, 214110 (2020).
- [20] F. Zhang, B. Liu, C.-K. Yang, Y.-Y. Hu, H.-D. Zhang, Q.-G. Li, X.-P. Wang, Y.-Y. Zhang, Y.-G. Yang, and L. Wei, Characterization of temperature-dependent superlattice in Cu:KTN crystal, *Mater. Res. Express* **7**, 126202 (2020).
- [21] F. Di Mei, L. Falsi, M. Flammini, D. Pierangeli, P. Di Porto, A. J. Agranat, and E. DelRe, Giant broadband refraction in the visible in a ferroelectric perovskite, *Nat. Photonics* **12**, 734 (2018).
- [22] M. Ferraro, D. Pierangeli, M. Flammini, G. Di Domenico, L. Falsi, F. Di Mei, A. J. Agranat, and E. DelRe, Observation of polarization-maintaining light propagation in depoled

- compositionally disordered ferroelectrics, *Opt. Lett.* **42**, 3856 (2017).
- [23] K. Du, M. Zhang, C. Dai, Z. N. Zhou, Y. W. Z. Xie, H. Ren, H. Tian, L. Q. Chen, G. Van Tendeloo, and Z. Zhang, Manipulating topological transformations of polar structures through real-time observation of the dynamic polarization evolution, *Nat. Commun.* **10**, 4864 (2019).
- [24] K. Christensen and N. R. Moloney, *Complexity and Criticality* (Imperial College Press, London, 2005).
- [25] K. Falconer, *Fractal Geometry: Mathematical Foundations and Applications*, 3rd ed. (John Wiley & Sons, New York, 2014).
- [26] M. Rams and K. Simon, The geometry of fractal percolation, in *Geometry and Analysis of Fractals*, edited by D. J. Feng and K. S. Lau, Springer Proceedings in Mathematics & Statistics Vol. 88 (Springer, New York, 2014).
- [27] K. Falconer and X. Jin, Self-similar sets: Projections, sections and percolation, in *Recent Developments in Fractals and Related Fields. FARF3 2015*, edited by J. Barral and S. Seuret, Trends in Mathematics (Birkhuser, Cham, 2017).
- [28] B. B. Mandelbrot, *The Fractal Geometry of Nature* (W.H. Freeman and Company, San Francisco, 1983).
- [29] Y. Feldman, A. Puzenko, and Y. Ryabov, Dielectric relaxation phenomena in complex materials, in *Fractals, Diffusion, and Relaxation in Disordered Complex Systems*, edited by S. A. Rice, W. T. Coffey, and Y. P. Kalmykov (2006), <https://doi.org/10.1002/0471790265.ch1>.
- [30] X. Zhang, Q. X. Yang, H. L. Liu, X. P. Wang, S. He, X. J. Li, and P. F. Wu, Switching effects of spontaneously formed superlattices in relaxor ferroelectrics, *Opt. Mater. Express* **9**, 4081 (2019).
- [31] Q. Yang, X. Zhang, H. Liu, X. Wang, Y. Ren, S. He, X. Li, and P. Wu, Dynamic relaxation process of a 3D super crystal structure in a Cu:KTN crystal, *Chin. Optic. Lett.* **18**, 021901 (2020).
- [32] L. E. Cross, Relaxor ferroelectrics: An overview, *Ferroelectrics* **151**, 305 (1994).
- [33] G. Burns and F. H. Dacol, Crystalline ferroelectrics with glassy polarization behavior, *Phys. Rev. B* **28**, 2527 (1983).
- [34] V. Westphal, W. Kleemann, and M. D. Glinchuk, Diffuse Phase Transitions and Random-Field-Induced Domain States of the Relaxor Ferroelectric, *Phys. Rev. Lett.* **68**, 847 (1992).
- [35] J. F. Scott, Applications of modern ferroelectrics, *Science* **315**, 954 (2007).
- [36] J. Wang, K. Nagano, T. Shimada, and T. Kitamura, Strain-mediated multilevel ferroelectric random access memory operating through a magnetic field, *RSC Adv.* **4**, 45382 (2014).